



Article

# Enhanced Nutrient Removal in A<sub>2</sub>N Effluent by Reclaimed Biochar Adsorption

Peng Chen <sup>1</sup>, Junkang Wu <sup>1,2,\*</sup>, Yue He <sup>3</sup>, Yaping Zhang <sup>1</sup>, Ran Yu <sup>1</sup>  and Xiwu Lu <sup>1,\*</sup>

- <sup>1</sup> Department of Environmental Science and Engineering, School of Energy and Environment, Wuxi Engineering Research Center of Taihu Lake Water Environment, Southeast University, Nanjing 210096, China; 230149616@seu.edu.cn (P.C.); amflora@seu.edu.cn (Y.Z.); yuran@seu.edu.cn (R.Y.)
- <sup>2</sup> Department of Water Supply and Drainage Science and Engineering, College of Civil Engineering, Nanjing Forestry University, Nanjing 210037, China
- <sup>3</sup> Nanjing Institute of Environmental Sciences, Ministry of Ecology and Environment, Nanjing 210042, China; heyue@nies.org
- \* Correspondence: wjkang@njfu.edu.cn (J.W.); xiwulu@seu.edu.cn (X.L.)

**Abstract:** The excessive nitrogen and phosphorus discharged into the water environment will cause water eutrophication and thus disrupt the water ecosystem and even exert biological toxicities. In this study, the absorption removal of nitrogen and phosphorus from the anaerobic tank in an anaerobic–anoxic/nitrifying system using four different kinds of biowaste-reclaimed biochars were investigated and compared. The effects of temperature and pH on nutrient adsorption removal were further investigated. The four kinds of biochar were successfully prepared and well characterized using a scanning electron microscope, fourier transform infrared spectroscopy, X-ray diffraction and Brunner–Emmet–Teller methods. Generally, there was no significant change in chemical oxygen demand (COD) and NH<sub>4</sub><sup>+</sup>-N removal efficiencies when treated by the different biochars, while the activated sludge biochar (ASB) displayed the highest total phosphorus (TP) removal efficiency. The initial TP concentrations (<40 mg/L) displayed no remarkable effects on the TP adsorption removal, while the increase of temperature generally enhanced TP and NH<sub>4</sub><sup>+</sup>-N adsorptions on the ASB. Besides, the increase of pH significantly promoted NH<sub>4</sub><sup>+</sup>-N removal but depressed TP removal. Moreover, the adsorption process of TP by the ASB complies with the secondary kinetic model, suggesting the chemical precipitation and physical electrostatic interaction mechanisms of TP adsorption removal. However, the adsorption of NH<sub>4</sub><sup>+</sup>-N conformed to the inner-particle diffusion model, indicating that the NH<sub>4</sub><sup>+</sup>-N adsorption was mainly involved with pore diffusions in the particles.



**Citation:** Chen, P.; Wu, J.; He, Y.; Zhang, Y.; Yu, R.; Lu, X. Enhanced Nutrient Removal in A<sub>2</sub>N Effluent by Reclaimed Biochar Adsorption. *Int. J. Environ. Res. Public Health* **2022**, *19*, 4016. <https://doi.org/10.3390/ijerph19074016>

Academic Editor: Yung-Tse Hung

Received: 2 March 2022

Accepted: 25 March 2022

Published: 28 March 2022

**Publisher's Note:** MDPI stays neutral with regard to jurisdictional claims in published maps and institutional affiliations.



**Copyright:** © 2022 by the authors. Licensee MDPI, Basel, Switzerland. This article is an open access article distributed under the terms and conditions of the Creative Commons Attribution (CC BY) license (<https://creativecommons.org/licenses/by/4.0/>).

**Keywords:** nitrogen and phosphorus; biochar; activated sludge; adsorption; temperature; pH

## 1. Introduction

Nitrogen and phosphorus are essential nutritional sources for biological growth. However, the excessive nutritional salt content of nitrogen and phosphorus in water bodies will cause water quality pollution phenomenon, that is, water eutrophication [1–3]. It is caused by the imbalance of the input and output of nutrient and thus disrupt the water ecosystem balance. The quick reproduction of algae and phytoplankton, forming blooms and red tide in the surface water [4], will destroy the balance of dissolved oxygen in the water environment and disrupt the flow of material and energy in the system [1,2]. Oxytoxin will cause biological poisoning in the water and make the whole water ecosystem gradually perish.

The discharge of urban domestic sewage is the main source of nitrogen and phosphorus in natural water bodies. It is also an important reason for the eutrophication of the lake water. In recent decades, with the rapid economic development and the continuous improvement of the urbanization rate, the production of urban sewage has increased by

5–8% in China [5]. Currently, the nutrients in the wastewater are mainly removed using biological treatment methods by microorganisms [6]. However, the traditional biological nutrient removal technology has many deficiencies, such as the insufficient carbon source, the competition between phosphorus accumulating organisms and denitrifiers for carbon source, and the contradiction of sludge retention time while conducting simultaneous nitrogen and phosphorus removal [7,8]. In addition, phosphorus is considered a non-renewable and strategic resource. Therefore, it is of great significance to develop new processes to realize efficient nutrient removal as well as phosphorus recovery.

In view of the deficiencies of traditional biological wastewater treatment, a new process of the anaerobic–anoxic/nitrifying/induced crystallization (A<sub>2</sub>N-IC) recovery has been previously proposed by our research group [9,10]. This process can not only significantly improve the efficiency of nitrogen removal but also realize the effective recovery of phosphorus resources and reduce the energy consumption of sewage treatment [11]. However, the effect of induced crystallization is greatly influenced by the phosphorus concentration of the anaerobic pool [10]. The phosphorus with concentrations as low as 0.35 mg/L in the anaerobic pool was not well recovered when using induced crystallization methods. Compared with the chemical crystallization, the biochar adsorption method is expected to display more advantages while under the condition of low phosphorus concentrations [12]. The adsorption saturated biochar can also be used for soil improvement and increase of fertilization effect, to realize the resource utilization of nitrogen and phosphorus [13,14].

As the by-product and the biowaste during biological wastewater treatment, the urban sewage sludge has already exceeded 30 million tons in production in 2018 [5]. At present, sludge treatment methods mainly include landfill, land use, building materials utilization, and incineration [15]. It requires large investment and consumption of building materials during transportation, storage and treatment of sludge biowaste. The low-temperature heating transformations of activated sludge into biochar as soil modification can remarkably decrease the treatment costs [16,17]. Meanwhile, the sludge biochar can improve the physical and chemical properties of soil and improve soil ecology [18,19]. Thus, in this study, the sludge biowaste was considered as the potential biochar to adsorb the nutrients in the A<sub>2</sub>N effluent. The adsorption-saturated biochar containing N and P for soil modification were expected to be beneficial for crop growth and can increase the number of exchangeable cations in the soil and provide the element supply source [20,21].

The objective of this study is to compare the adsorption removal of N and P from the anaerobic pool in A<sub>2</sub>N system using different kinds of biochar. The effects of temperature and pH on nutrient adsorption removal were further investigated, as well as the adsorption characteristics and mechanisms. The study mainly includes: (1) Preparation and characterization of four kinds of biochar and comparison of adsorption removal effect of N and P; (2) Adsorption dynamics and isotherm analysis of the selected biochar; and (3) Influences of different initial concentration, reaction time, reaction temperature and pH on N and P adsorption removal and the potential influence mechanisms.

## 2. Materials and Methods

### 2.1. Preparation of the Biochar

A three-stage reaction vacuum atmosphere furnace was used to prepare the biochar, and the temperature layer was stabilized in the middle section through a three-stage heating method to produce finer biochar. The raw materials used in the experiment were wheat straw, applewood branches, China fir branches and activated sludge from Nanjing Chengdong wastewater treatment plant (Capacity: 200,000 m<sup>3</sup>/d; Coordinates: 32°00′00″ N, 118°51′36″ E). The raw materials were dried in oven at 60 °C, then crushed to 2 mm using an LFP-800 crusher, and finally screened for the following experiments. Five grams of the pretreated crushing raw material was used for biochar manufacture in the tube furnace. The middle section of the tube furnace was blocked with asbestos prior to pyrolyzation with aeration of nitrogen gas at a rate of 0.5 L/min. The heating rate and retention time were

maintained at 10 °C/min and 1 h. After the temperature dropped to 25 °C, the samples were withdrawn from the carbonization furnace and then ground for characterization.

## 2.2. Biochar Characterization

The structural properties of biochar surfaces were characterized using emission scanning electron microscope (SEM), fourier transform infrared (FTIR) spectroscopy, X-ray diffraction (XRD) and Brunner-Emmet-Teller (BET) measurements. After drying the four biochar samples and spraying gold, the biochar surface structure was observed using a high-resolution field emission scanning electron microscope (SEM, SU8010, Hitachi, Tokyo, Japan). The energy spectrometer EDS (Oxford 7582, Oxford Instruments, Concord, MA, USA) was used for the metal analysis on the biochar surface. The surface functional group of biochar samples were analyzed using a FTIR spectroscopy (Nicolet IS50, Thermo Scientific, Waltham, MA, USA). The Wavenumber was in the range of 4000–400  $\text{cm}^{-1}$ . The scanning times were performed at 32 with a resolution of 4  $\text{cm}^{-1}$ . The specific surface area and pore diameter of biochar were determined using a BET analyzer (BSD-PS1/2/4, BSD Instrument, Beijing, China). Biochar crystal analysis was performed using the XRD (X-ray diffraction). The crystal structures of the biochar powder samples were analyzed using a Brooke XRD instrument (Bruker D8 advance, Bruker, Germany). The ray wavelength, voltage, and current were set as 0.15406 nm, 40 kV, and 40 mA, respectively. The XRD peak was identified using the origin software.

## 2.3. Wastewater Contaminates Adsorption and Degradation Test

Synthetic wastewater simulating the effluent of the anaerobic tank in the  $\text{A}_2\text{N}$  system was used for the adsorption and degradation test. The sodium acetate, potassium dihydrogen phosphate and ammonium bicarbonate were used for synthetic wastewater to reach a final chemical oxygen demand (COD) concentration of 50 mg/L, total phosphorus (TP) concentration of 30 mg/L and  $\text{NH}_4^+\text{-N}$  concentration of 30 mg/L. The details of the trace metals were available in our previous studies [9,10]. One hundred milliliters of the synthetic sewage was put into a 250 mL flask and the initial pH was adjusted to 7 using HCl/NaOH solutions. After adding 0.3 g of the four biochar, the flasks were shaken at 150 rpm at room temperature. Samples were taken at 9, 12, 15, 20, 25, 30, 40, 70, 130 and 250 min and then filtered using a 0.45  $\mu\text{m}$  filter for COD, TP and  $\text{NH}_4^+\text{-N}$  measurement.

## 2.4. Temperature and pH Influence Test

One hundred milliliters of wastewater containing 50 mg/L COD and different concentrations of nutrients (concentrations setup seen in Table 1) were taken for adsorption test under three different temperature conditions of 288 K, 298 K and 308 K, respectively. The initial pH of the solution was kept around 7. For pH test, the initial COD,  $\text{NH}_4^+\text{-N}$  and TP concentrations were set as 50 mg/L, 30 mg/L, and 30 mg/L, respectively. The initial pH of each reaction system adjusted by HCl or NaOH solutions was kept as 2, 3, 4, 5, 6, 7, 8, 9, 10, 11 and 12, respectively. A 0.3 g of activated sludge biochar (ASB) was added into each 250 mL flask containing 100 mL wastewater for shaking at 150 rpm. After 4 h and 8 h of reaction, the  $\text{NH}_4^+\text{-N}$  and TP concentrations were measured.

**Table 1.** Concentrations Setup of  $\text{NH}_4^+\text{-N}$  and TP Adsorption Test.

Name	Test 1	Test 2	Test 3	Test 4	Test 5	Test 6
$\text{NH}_4^+$ adsorption test						
$\text{NH}_4^+\text{-N}$ (mg/L)	30	30	30	30	30	30
TP (mg/L)	14	18	22	26	30	34
TP adsorption test						
$\text{NH}_4^+\text{-N}$ (mg/L)	15	20	25	30	35	40
TP (mg/L)	30	30	30	30	30	30

Notes: TP: Total phosphorus.

### 2.5. Chemical Analysis

COD,  $\text{NH}_4^+$ -N, and TP concentrations were determined according to the standard methods [22]. pH was measured using a pH meter (HACH SC200, HACH, Loveland, CO, USA).

### 2.6. Analysis of Adsorption Kinetics and Adsorption Isotherm

The Pseudo-first order kinetic equations, Pseudo-second order kinetic and internal diffusion models [23–25] were applied for curve fitting of adsorption kinetics of TP and  $\text{NH}_4^+$ -N by the ASB. The fitting equations were as follows:

The first-order kinetic equation:

$$\frac{dQ_t}{dt} = K_1(Q_e - Q_t) \quad (1)$$

The second-order kinetic equation:

$$\frac{dQ_t}{dt} = K_2(Q_e - Q_t)^2 \quad (2)$$

Internal diffusion model:

$$Q_t = K_3 t^{0.5} + b \quad (3)$$

where:  $Q_e$ —the equilibrium adsorption capacity, mg/g;

$Q_t$ —the adsorption capacity at time t, mg/g;

$K_1$ —the first adsorption rate constant;

$K_2$ —the second adsorption rate constant;

$K_3$ —the inter-diffusion constant between particles.

The calculation formula of the adsorption quantity  $Q$  is:

$$Q = \frac{(C_0 - C_e)V}{m} \quad (4)$$

where:  $C_0$ —the initial TP or  $\text{NH}_4^+$ -N concentration, mg/L;

$C_e$ —the TP or  $\text{NH}_4^+$ -N concentration when reaching adsorption equilibrium, mg/L;

$V$ —the reaction volume, L;

$m$ —the added biochar mass, g.

The Langmuir and Freundlich equations were applied for curve fitting after 4 h and 8 h adsorption reaction shown as follows:

The Langmuir isothermal equation:

$$Q = \frac{K_L Q_m C_e}{1 + K_L C_e} \quad (5)$$

The Freundlich isothermal equation:

$$Q = k_F C_e^n \quad (6)$$

where:  $Q$ —the adsorption capacity, mg/g;

$C_e$ —the TP or  $\text{NH}_4^+$ -N concentration when reaching equilibrium, mg/L;

$Q_m$ —the maximum equilibrium adsorption capacity, mg/g;

$K_L$ —the Langmuir constant;

$K_F$ —Freundlich constant.

### 3. Results and Discussions

#### 3.1. Biochar Characteristics

##### 3.1.1. SEM-EDS

SEM imaging with four different scanning ranges of the prepared biochars was shown in Figure 1. It can be seen that the surface morphology of the ASB is significantly different from that of the three other plant biochars. The surface morphology and structure of the biochars are highly related to the characteristics of the raw materials. The straw biochar (STB), applewood biochar (AWB), and China fir biochar (CFB) displayed a fiber structure on the surface, which accorded with the structure of the raw materials [26]. Uneven distribution of pore size and irregular cracks were observed on the STB surface (Figure 1a). The AWB displayed a smooth surface and parallel round hole shape structure (Figure 1b). In addition, the CFB had a dense pore distribution and a large pore size, and an obvious layered structure was determined (Figure 1c). Instead of having the fiber structure, the ASB presented a relatively large and compact particulate structure, probably due to the carbonization of organic matter in the sludge (Figure 1d). Moreover, the ASB surface is rough with the presence of irregular granular carbon, and the pore distribution was disordered. This might be due to the carbonization and excessive fragmentation of the organic matter in the sludge (Figure 1d). Cheng et al. have also reported similar ASB characteristics as observed in this study [27].

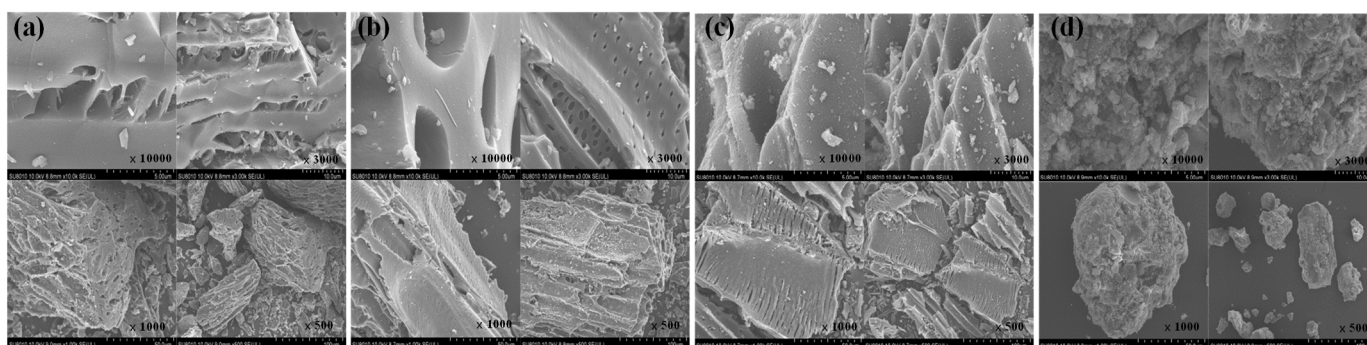


**Figure 1.** SEM morphology of four kinds of biochar: (a) Straw biochar; (b) Applewood biochar; (c) China fir biochar; (d) Activated sludge biochar.

The results of the energy profiles of the four different biochars are shown in Figure 2 to obtain the element components in the biochar. The STB surface was rich in carbon and oxygen elements, with atomic mass scores of 77.3% and 12.9%, respectively, in addition to the elements of P, K, Ca, and Mg (Figure 2a). Instead, the elements on the AWB surface were not as rich as those on the STB. The carbon element amount dominated in AWB as high as 96.1%, followed by the oxygen element accounting for 2.9% (Figure 2b). The element components in the CFB were similar to the AWB (Figure 2b,c). In addition, the ASB had the lowest carbon content as low as 10% when compared with the other three biochars but was the one most rich in element types—as many as 12 species (Figure 2d). The most abundant element in the ASB was the oxygen element, accounting for 50%, followed by silicon element (20%). Moreover, there were several metal elements with low abundance including Mg, Al, K, Ca, Fe, etc. Many studies have reported that the carbon and potassium content in non-cellulosic biochar are lower than that in cellulose biochar, while Ca, Mg, Al and other elements are higher than that in cellulose biochar [28–30], which was in accordance with the EDS results obtained in our study.

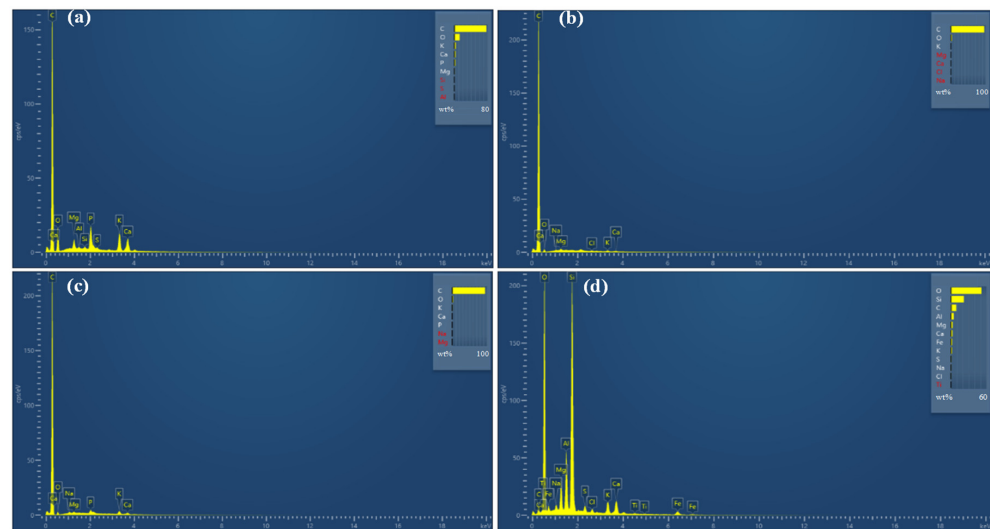


**Figure 2.** EDS spectrum of four kinds of biochar: (a) Straw biochar; (b) Applewood biochar; (c) China fir biochar; (d) Activated sludge biochar.

### 3.1.2. FTIR

The functional group profiling of the biocarbon surface was obtained by FTIR analysis as shown in Figure 3. It can be seen that the four biochars have similar characteristic absorption peaks and thus similar functional groups on the surface. The AWB and CFB show a highly consistent absorption peak, indicating that the raw material composition of the AWB and CFB was very similar. There are three obvious characteristic peaks in the spectrum with wavenumbers of 3430, 1424 and 1105  $\text{cm}^{-1}$  (Figure 3a). The ASB had the largest adsorption peak at 3430  $\text{cm}^{-1}$ , which is caused by O-H telescopic vibration indicating the phenol and alcohol hydroxyl functional group [31]. The absorption peak at 1424  $\text{cm}^{-1}$  is caused by C=C stretching vibration, and the peak near 1105  $\text{cm}^{-1}$  is mainly attributed to C–O–C antisymmetric stretching vibration [32,33]. In addition, the peak at 1586  $\text{cm}^{-1}$  is due to the aromatized C=C stretching vibration [34] and multiple aromatic C–H deformation vibration was also observed at the peaks of 600–800  $\text{cm}^{-1}$  [35], including 796 and 879  $\text{cm}^{-1}$  peaks. Therefore, the presence of aromatic compounds was available in all four biochars. The STB and CFB have also been characterized to contain hydroxyl group, aromatic structure and carboxyl group but without ether functional groups by FTIR spectroscopy analysis [36], which is consistent with the main functional groups obtained in this study. In summary, the four biochars had the hydroxy and ether functional groups and aromatic structures, and the ASB was minimally aromatized.

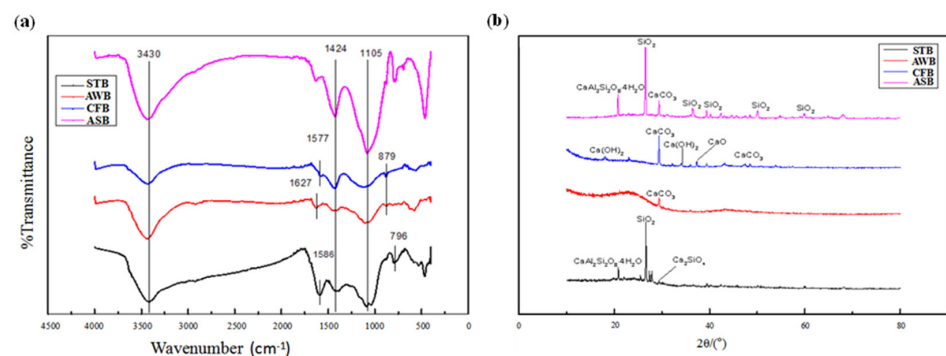


**Figure 3.** Fourier transform infrared (a) and X-ray diffraction (b) spectra of the four biochars.

### 3.1.3. XRD

The X-ray diffraction profiles of four different biochars were shown in Figure 3b. It can be seen that the STB and the ASB had an obvious peak at  $26.6^\circ$  and the AWB and CFB had a peak at  $29.4^\circ$  (Figure 3b). The highest peak at  $26.6^\circ$  in the ASB has been also documented as  $\text{SiO}_2$ , as well as the presence of metal oxides, including  $\text{CaCO}_3$ ,  $\text{CaO}$  and  $\text{MgO}$  [37,38], which was similar to the XRD and EDS results in this study. In addition, the strength of the STB and the ASB diffraction peak is relatively high than the others, indicating the high crystallization performance of the STB and the ASB. The high crystallization of biochar has been reported to display better adsorption performance and high stability [39]. Therefore, the ASB was expected to exert the best adsorption performance. In addition, there are multiple diffraction peaks occurring in the CFB and ASB between  $40^\circ$  and  $70^\circ$ , indicating that the ASB and CFB surfaces are mineralized with a certain amount of mineral composition.

### 3.1.4. BET

The specific surface area and porosity of biochar are critical for its adsorption properties, which was determined using BET method in this study. The  $\text{N}_2$  adsorption–desorption curves of the four biochars were shown in Figure 4. According to the International Union of Pure and Applied Chemistry (IUPAC) classification, the adsorption–desorption curves of the ASB and STB belong to the II type curve, while those of the CFB and AWB belong to the type I curve. In the CFB and AWB, there are obvious microporous monolayer adsorption features in the low relative pressure region, and an extension at the relative pressures of 0.1–0.3 and 0.5–0.9 was observed. It can be inferred from the curve that the pore of the AWB and the CFB was mainly slit shaped. In addition, the adsorption capacity rapidly increased under low relative pressure and thus caused a convex shape of the curve in the ASB and STB, probably due to the strong interaction between the adsorbate and the biochar surface.

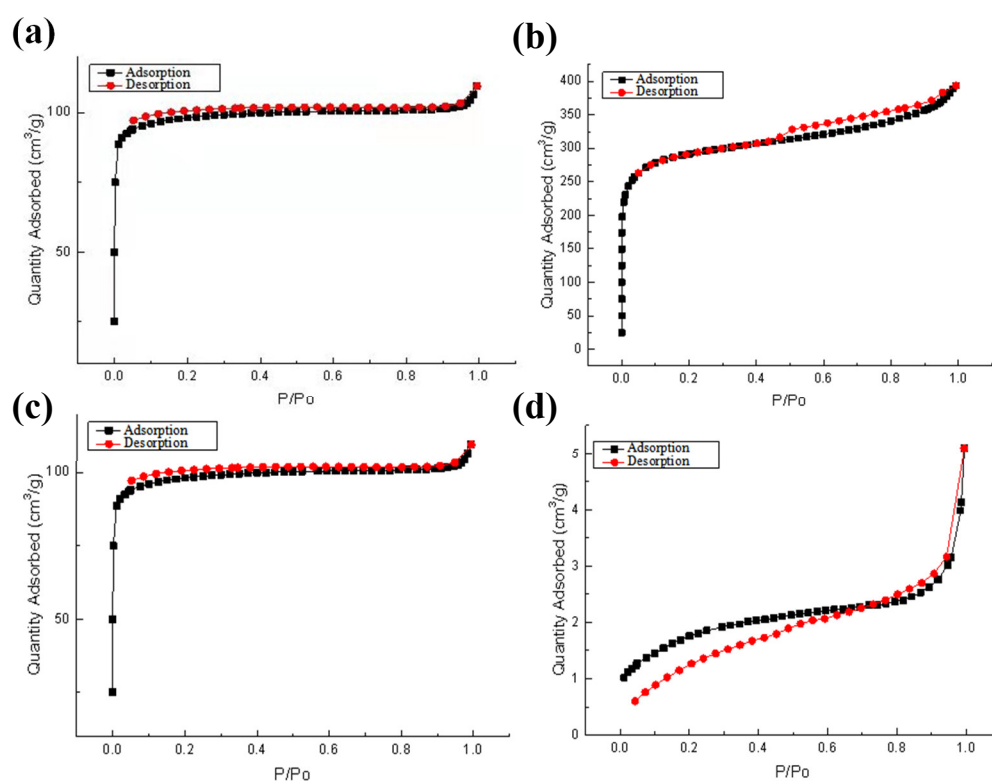


**Figure 4.**  $\text{N}_2$  adsorption–desorption curve of four kinds of biochar: (a) Straw biochar; (b) Applewood biochar; (c) China fir biochar; (d) Activated sludge biochar.

The specific surface area and pore size of four kinds of biochar were shown in Table 2. The average pore diameter of the four biochars was similar, in the range of 4.56–6.49 nm (Table 2). The order of the specific surface area of the four biochars is: CFB >> AWB > ASB >> STB, and the specific surface area size is consistent with the SEM imaging results. The specific surface area of biochar is related to the type of raw materials and the volatile components contained. During the preparation of biochar, the volatilization facilitates the formation of pore structure, and cellulosic biomass has rich internal pore [40,41], which might result in the high specific surface area of CFB and AWB. The specific surface area of CFB reached 1116.13 m<sup>2</sup>/g and had a pore capacity of 0.338 cm<sup>3</sup>/g, indicating that the CFB might probably display good physical adsorption capacity.

**Table 2.** Specific Surface Area and Pore Size of Four Kinds of Biochar.

Biochar	Specific Surface Area (m <sup>2</sup> /g)	Micropore Surface Area (m <sup>2</sup> /g)	Total Pore Volume (cm <sup>3</sup> /g)	Micropore Volume (cm <sup>3</sup> /g)	Average Pore Size (nm)	Iodine Sorption Value (mg/g)
STB	6.3958	0.7819	0.0048	0.0002	6.2728	287
AWB	391.0390	353.8750	0.1583	0.1353	4.7700	285
CFB	1116.1316	860.9206	0.5726	0.3384	4.5637	1115
ASB	123.3406	60.6806	0.0995	0.0256	6.4946	187

Notes: STB: Straw biochar; AWB: Applewood biochar; CFB: China fir biochar; ASB: Activated sludge biochar.

### 3.2. Adsorption Removal of COD, TP and NH<sub>4</sub><sup>+</sup>-N

Generally, there was no significant change in COD and NH<sub>4</sub><sup>+</sup>-N variations between the four biochar tests. As shown in Figure 5a,c, the COD and NH<sub>4</sub><sup>+</sup>-N removal efficiencies all rapidly increased within 0.5 h. With the prolonged reaction time (0.5–4 h), there was an obvious fluctuation in COD removal in all the adsorption tests, while the NH<sub>4</sub><sup>+</sup>-N removal rates gradually reached stable. The fluctuation in COD removal might be attributed to the biochar dissolution and COD release from the biochar. Odedishemi et al. [42] determined that the dissolved organic carbon release from the biochar in a constructed wetland and the COD could actually be utilized by the microorganisms. The highest COD removal efficiencies by the AWB, CFB, ASB and STB were achieved at 99.6%, 91.8%, 97.5% and 96.6%, respectively (Figure 5a). After 4 h of reaction, the ASB displayed a slightly higher NH<sub>4</sub><sup>+</sup>-N removal efficiency of 62.4% than the other biochars with the NH<sub>4</sub><sup>+</sup>-N removal between 46.6–51.3% (Figure 5c).

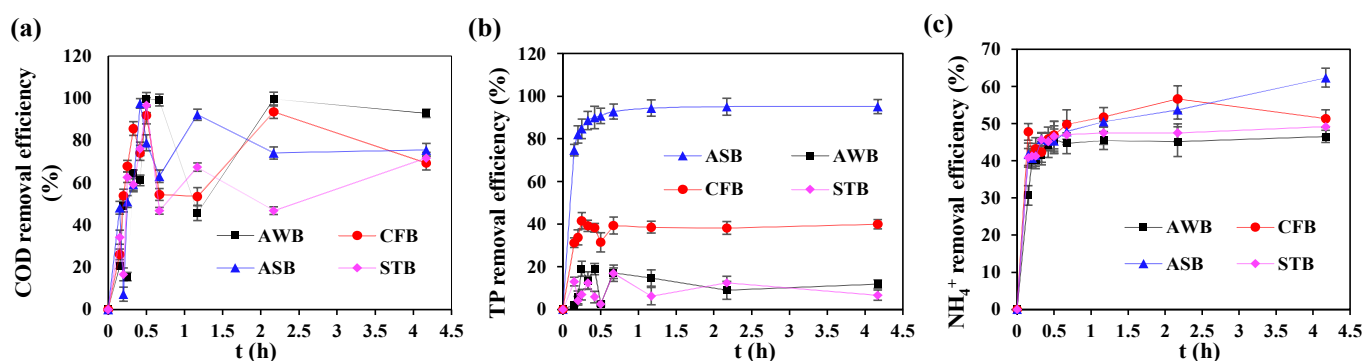


**Figure 5.** Adsorption effect of four kinds of biochar on: (a) COD; (b) TP and (c) NH<sub>4</sub><sup>+</sup>-N.

The TP adsorption effect varied significantly from different biochars. After 0.25 h of reaction, the TP removal efficiencies achieved by the AWB, CFB, STB and ASB rapidly reached at 19.1%, 41.6%, 12.5% and 84.7%, respectively (Figure 5b). After that, the TP removal gradually kept stable. In addition, the ASB exerted the highest TP adsorption removal rate of 95.1%, significantly higher than the AWB (11.9%), CFB (40.0%) and STB

(6.6%) (Figure 5b). sludge biochar shows a great advantage in TP adsorption. Thus, the ASB displayed higher TP removal efficiency than the other three biochars and was expected to play a critical role in enhanced P removal in A<sub>2</sub>N-IC system.

The mechanism of biochar adsorption of phosphate is well reported to include multiple reactions [24,43]. The biochar surface with a positive charge could interact with the phosphate anion by electrostatic interaction, which generally occurs at the beginning of the adsorption reaction [24]. In addition, the metal and the oxides on the biochar surface could react with the phosphate in the aqueous solution through precipitation to form stabilized precipitates [43]. Moreover, multivalent cations (e.g., Ca, Mg, Fe, and Al) in the biochar can chelate with phosphate to form composite minerals using oxygen-containing functional groups as bridge bonds. The abundant metal elements in the ASB by EDS analysis and the obtained phenol and alcohol oxyhydril functional groups by FTIR analysis previously further supported the potential precipitation and complexation reactions mechanisms of TP removal by the ASB. Therefore, the chemical adsorption reaction including electrostatic adsorption, surface precipitation and complex cooperation contributed to the excellent TP removal performances of the ASB in this study. The ASB will be selected for the following temperature and pH influencing test.

### 3.3. Effects of Temperature on Adsorption-Removal Efficiency

Generally, the TP concentrations displayed a similar variation trend when treated by the ASB at different temperatures as seen in Figure 6. After 4 h and 8 h of reaction, the TP was all remarkably removed by more than 86% and 90%, respectively, at all the three temperatures (Figure 6a–c), which indicated that the adsorption equilibrium might have been probably reached within 4 h. The increase of initial TP concentrations from 18 to 40 mg/L slightly depressed the TP removal efficiencies by 3.7%, 2.1% and 0.3% under 288 K, 298 K and 308 K conditions, respectively after 8 h of reaction (Figure 6). It is inferred that the initial phosphorus concentration below 40 mg/L had few effects on the adsorption efficiency. The increase of temperature generally enhanced the TP adsorptions on the ASB. The TP removal rate significantly increased from  $92.2 \pm 0.7\%$  to  $97.0 \pm 0.6\%$  when the temperature rose from 288 K to 308 K (Figure 6a–c).

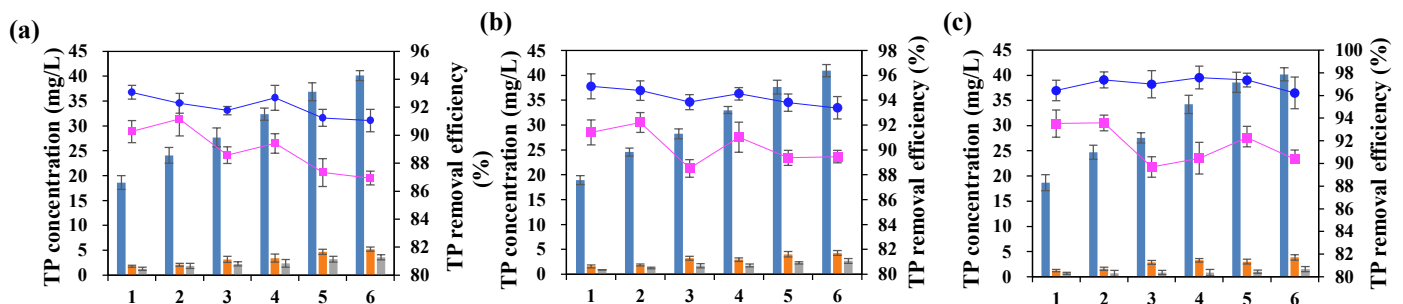


Figure 6. TP removal at different temperatures: (a) 288 K; (b) 298 K; (c) 308 K.

The NH<sub>4</sub><sup>+</sup>-N removal remarkably varied from the initial concentrations, the reaction time and the temperatures, as seen in Figure 7. The NH<sub>4</sub><sup>+</sup>-N removal was kept stable at  $48.2 \pm 3.9\%$  after 4 h of reaction regardless of the initial NH<sub>4</sub><sup>+</sup>-N concentrations and the temperatures. Nevertheless, the NH<sub>4</sub><sup>+</sup>-N removal rate increased by  $36.9 \pm 5.0\%$  after 8 h of reaction and displayed a significantly positive relation to the initial NH<sub>4</sub><sup>+</sup>-N concentrations at all three temperatures. Therefore, the NH<sub>4</sub><sup>+</sup>-N reached the adsorption equilibrium only after 8 h of reaction, longer than that than when the TP reached adsorption equilibrium. In addition, the increase of temperature from 288 K to 308 K dramatically enhanced the NH<sub>4</sub><sup>+</sup>-N removal from  $61.2 \pm 6.7\%$  to  $73.2 \pm 5.4\%$ , suggesting that the high temperature is conducive to the adsorption reaction and the removal of ammonia nitrogen.

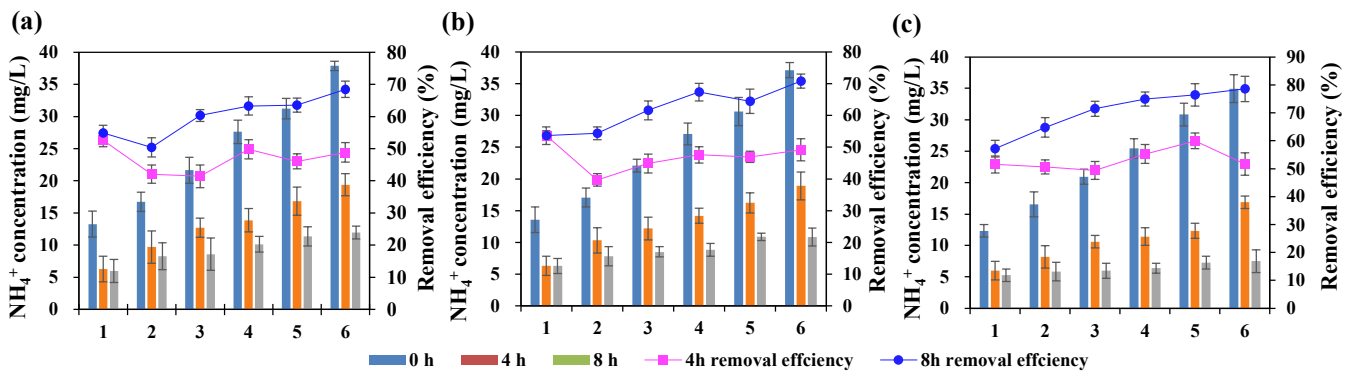


Figure 7.  $\text{NH}_4^+\text{-N}$  removal efficiency at different temperatures: (a) 288 K; (b) 298 K; (c) 308 K.

3.4. Effects of pH on Adsorption-removal Efficiency

The effect of initial pH on the TP adsorption removal is shown in Figure 8a,b. The adsorption removal of TP in wastewater firstly increased from 84.1% to 96.2% when pH increased from 2 to 5, then gradually decreased, and a significant reduction in the removal efficiency to around 45.2% was observed when pH higher than 9. The corresponding adsorption capacity increased from 4.2 mg/g to 5.1 mg/g, and then decreased only to 2.2 mg/g. Therefore, the increase of pH under faintly acid conditions would promote TP adsorption by ASB, while the high alkalinity might exert notable adverse effects on TP adsorption.

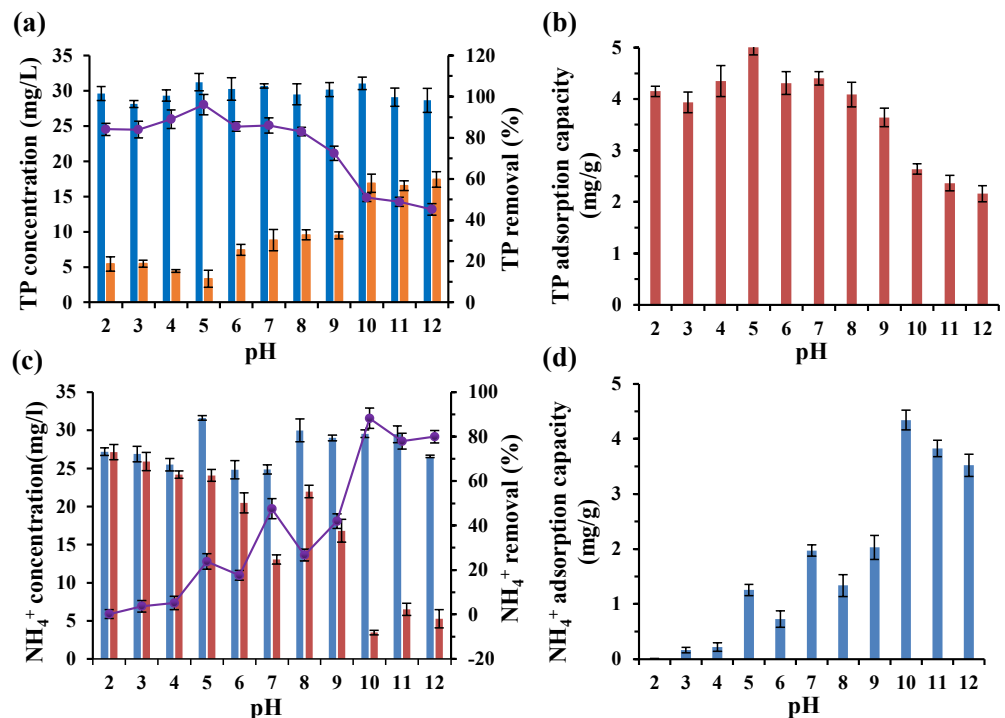


Figure 8. Effect of pH on the removal rate and the adsorption capacity of TP (a,b) and  $\text{NH}_4^+\text{-N}$  (c,d), respectively.

The form of P in the water and biochar surface charge under different pH conditions would be probably responsible for the varying adsorption efficiencies. Generally, P present in the water is a form of  $\text{PO}_4^{3-}$ ,  $\text{HPO}_4^{2-}$  and  $\text{H}_2\text{PO}_4^-$ , with the equilibrium constants of 2.15, 7.20 and 12.33, respectively [44]. P is mainly in the form of anionic  $\text{H}_2\text{PO}_4^-$  with pH at 2–7. Meanwhile, the pH value in the wastewater will affect the ASB surface charge [45]. When the pH value in wastewater is less than zero-point charge (zeta potential), the protonation

of ASB chemicals could lead to a positive charge on the surface. The zero-point charge (zeta potential) of the ASB was measured as 5.46. The adsorption removal was, therefore, expected to increase due to the electrostatic attraction between  $\text{H}_2\text{PO}_4^-$  and OH group (Figure 3a) on the ASB surface confirmed by FTIR analysis above, and the adsorption performance gradually decreased when pH was higher than 5. In addition, when pH increased higher to 10, P is mainly in the form of  $\text{HPO}_4^{2-}$  and  $\text{OH}^-$  would be abundant in the wastewater, which might probably compete with  $\text{HPO}_4^{2-}$  for adsorption on the positively charged ASB surface.

The effect of initial pH on the adsorption removal of  $\text{NH}_4^+$ -N is shown in Figure 8c,d. When the pH increased from 2 to 12, the adsorption removal of  $\text{NH}_4^+$ -N by ASB significantly increased by around 80%. It has been well-known that the ammonia nitrogen in the wastewater is mainly in the form of  $\text{NH}_4^+$  when the solution is under acidic conditions [46]. Thus, the positively charged  $\text{NH}_4^+$  would probably repel to ASB surface with a positive charge and compromised the adsorption effect. With the decrease of  $\text{H}^+$  concentration and increase of  $\text{OH}^-$  concentration as pH rising, ammonia nitrogen in the wastewater began to be in the form of free  $\text{NH}_3$  and the electrostatic attraction between  $\text{NH}_3$  and ASB gradually enhanced, which finally resulted in the high adsorption capacity of  $\text{NH}_4^+$ -N. The adsorption capacity of ammonia nitrogen increased from 1.97 mg/g to 4.34 mg/g by 120% when pH ranging from 7 to 10.

### 3.5. Adsorption Dynamics and Adsorption Isotherm

The TP adsorption process was relatively more in line with the Pseudo-second order and Pseudo-first order model, with the correlation coefficient of 0.9623 and 0.9351, respectively, which is significantly higher than that (0.4716) of the internal diffusion model (Table 3 and Figure 9). The Pseudo-first order kinetic model was suitable for fitting at the beginning of the adsorption reaction rather than the substrate transmission period. The Pseudo-second kinetic model includes liquid membrane diffusion, internal diffusion and surface adsorption, and the adsorption process is mainly controlled by chemical action, such as electron sharing or electron transfer and broken chemical bond and generation [47,48]. As discussed above, the mechanisms of TP adsorption by the ASB mainly included chemical precipitation with metal oxide and electrostatic interaction on the surface [43,49]. The observed abundant metal elements (e.g., Ca, Mg and Fe) and oxygen-contained groups (e.g., phenol and alcohol hydroxyl group) on the ASB surface further supported the proposed adsorption removal mechanisms. In summary, the Pseudo-second kinetic model was expected to better describe the TP adsorption removal process by the ASB.

**Table 3.** Specific surface area and pore size of four kinds of biochar.

	Pseudo-First Order			Pseudo-Second Order			Intraparticle Diffusion		
	$K_1$ ( $\text{h}^{-1}$ )	$Q_{e1}$ (mg/g)	$R^2$	$K_2$ (g/(mg·h))	$Q_{e2}$ (mg/g)	$R^2$	$K_3$ (mg/(g·h))	$B$ (mg/g)	$R^2$
TP	10.3352	4.6149	0.9351	0.0866	4.8348	0.9623	0.4532	4.0074	0.4716
$\text{NH}_4^+$ -N	2.1923	7.9165	0.3579	5.3135	2.4004	0.7125	0.5297	1.5658	0.9653

The adsorption process of  $\text{NH}_4^+$  onto the ASB is mainly consistent with the intraparticle diffusion model with a correlation coefficient of 0.9653 (Table 3 and Figure 9b), significantly higher than that of the Pseudo-first or Pseudo-second kinetic model, indicating that the adsorption mechanisms were involved with physical diffusion from the particle surface through the internal pore. The porous structure of the ASB with compact and irregular granular particles determined by SEM imaging in Figure 1d might support the intraparticle diffusion process during the  $\text{NH}_4^+$  adsorption.

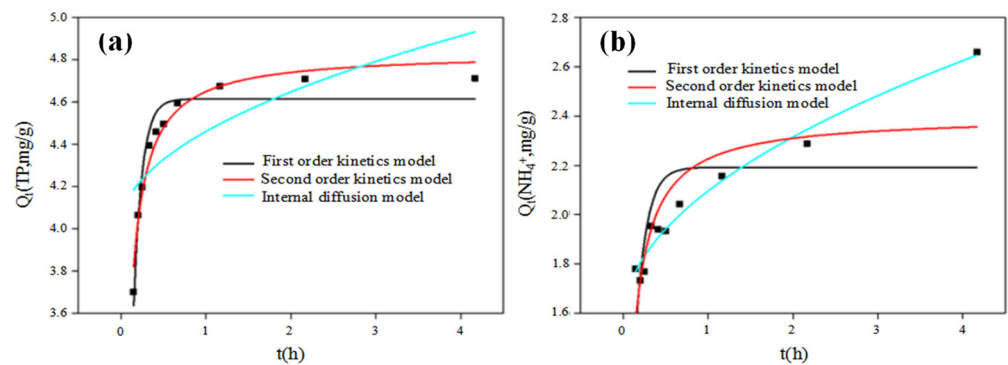


**Figure 9.** Adsorption kinetics fitting of TP (a) and  $\text{NH}_4^+\text{-N}$  (b) by the activated sludge biochar.

The Langmuir and Freundlich models [50] were finally applied for fitting the adsorption isotherm curve of TP and  $\text{NH}_4^+\text{-N}$ , as shown in Figure 10 and Table 4. Generally, an obvious S-type curve of TP and  $\text{NH}_4^+\text{-N}$  adsorption was observed, suggesting that at least two binding energy levels [51] occurred during the adsorption by the ASB. The Langmuir isothermal equation usually shows that the adsorbent is single-layer distributed on the adsorbent surface, while the Freundlich isothermal equation describes the multi-layer uneven adsorption and the adsorption capacity will increase with the increasing concentration [50]. In this study, similar correlation coefficients were obtained when fitting using Langmuir and Freundlich models (Table 4), which revealed that TP adsorption by dirty peat was probably a result of multiple processes, including both monolayer adsorption and multi-layer adsorption processes. In contrast, the Freundlich model could be used for fitting the curve of  $\text{NH}_4^+\text{-N}$  adsorption rather than the Langmuir model except for the 3 h of adsorption test at 35 °C (Table 4). It indicated that the adsorption of  $\text{NH}_4^+\text{-N}$  is mainly a process of multi-layer adsorption.

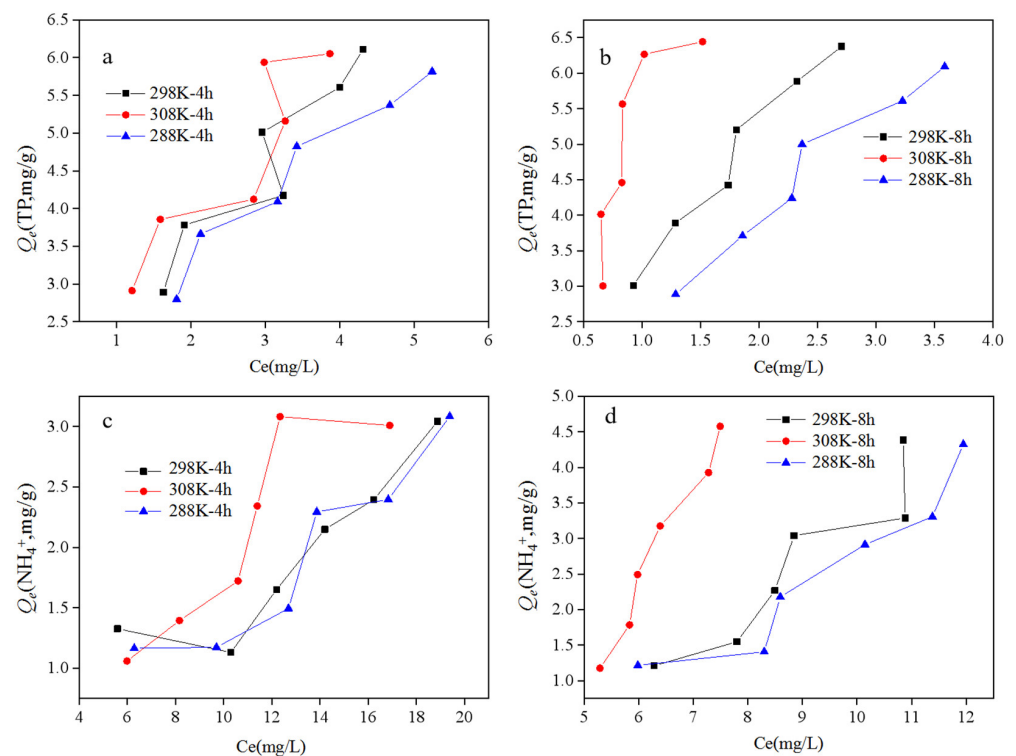


**Figure 10.** Adsorption isotherm curve of TP (a,b) and  $\text{NH}_4^+\text{-N}$  (c,d) by activated sludge biochar after 4 h and 8 h of reaction, respectively.

**Table 4.** Fitting parameters by Langmuir and Freundlich adsorption isotherms.

	Temperature	Time	Langmuir				Freundlich		
			$Q_m$ (mg g <sup>-1</sup> )	$K_L$ (L/mg)	$R_L$	$R^2$	$K_F$ (mg/g)	$N$	$R^2$
TP	288 K	4 h	11.2226	0.2020	0.2102	0.9468	2.1508	0.6025	0.9414
		8 h	16.4065	0.1643	0.2465	0.9589	2.4477	0.7186	0.9554
	298 K	4 h	13.3081	0.1821	0.2244	0.8408	16.0666	0.2286	0.8481
		8 h	15.9048	0.2486	0.1749	0.9658	3.2284	0.6965	0.9648
	308 K	4 h	10.3890	0.3319	0.1389	0.7406	2.7344	0.5730	0.7482
		8 h	14.8483	0.5657	0.0864	0.6320	5.2987	0.6401	0.5962
NH <sub>4</sub> <sup>+</sup> -N	288 K	4 h	-	-	-	-	0.1075	1.1174	0.8501
		8 h	-	-	-	-	0.0193	2.1540	0.9089
	298 K	4 h	-	-	-	-	0.1409	1.0227	0.7638
		8 h	-	-	-	-	0.0250	2.1166	0.8118
	308 K	4 h	68.5823	0.0029	0.9651	0.7493	0.1913	1.0048	0.7482
		8 h	-	-	-	-	0.0074	3.1919	0.9271

#### 4. Conclusions

In this study, the STB, AWB, CFB and ASB were successfully prepared and well-characterized. Generally, no significant change in COD and NH<sub>4</sub><sup>+</sup>-N variations were determined when treated by different biochars, while the ASB showed higher TP removal efficiencies than the others. The variations of initial phosphorus concentration did not remarkably affect the adsorption efficiency. In addition, the increase of temperature generally promoted the TP and NH<sub>4</sub><sup>+</sup>-N adsorptions on the ASB. the increase of pH notably enhanced NH<sub>4</sub><sup>+</sup>-N removal but decreased TP adsorption removal. What is more, the adsorption process of TP by the ASB was in line with the secondary kinetic model, reflecting the chemical precipitation and physical electrostatic interaction mechanisms of TP adsorption removal. In contrast, the process of NH<sub>4</sub><sup>+</sup>-N accorded with the inner-particle diffusion model, suggesting that the NH<sub>4</sub><sup>+</sup>-N adsorption process was mainly associated with pore diffusions in the particles.

**Author Contributions:** Conceptualization, P.C., and X.L.; methodology, P.C., Y.H. and Y.Z.; software, P.C. and J.W.; validation, P.C. and X.L.; formal analysis, P.C., J.W. and Y.Z.; investigation, P.C.; data curation, P.C. and Y.H.; writing—original draft preparation, P.C. and J.W.; writing—review and editing, P.C., J.W., R.Y. and X.L.; visualization, P.C., J.W. and Y.Z.; supervision, X.L.; project administration, X.L.; funding acquisition, X.L., R.Y. and J.W.; All authors have read and agreed to the published version of the manuscript.

**Funding:** This study was financially supported by the National Science and Technology Major Project (No. 2012ZX07101-005), National Natural Science Foundation of China (No. 51878145), Natural Science Foundation of Jiangsu Province (No. BK20200778), and Natural Science Foundation of the Higher Education Institutions of Jiangsu Province (No. 20KJB560035).

**Institutional Review Board Statement:** Not applicable.

**Data Availability Statement:** Data is contained within the article.

**Conflicts of Interest:** The authors declare no conflict of interest.

#### References

- Coimbra, K.T.O.; Alcântara, E.; de Souza Filho, C.R. Satellite evidence for pervasive water eutrophication in the Doce River reservoirs following the collapse of the Fundao dam in Brazil☆. *Environ. Pollut.* **2021**, *272*, 116014. [[CrossRef](#)] [[PubMed](#)]
- Zhou, L.; Wang, X.; Zhang, X.; Zhao, Y.; Zhu, P.; Zhao, X.; Li, X. Spatiotemporal variations in nitrogen and phosphorus in a large man-made lake and their relationships with human activities. *Water* **2020**, *12*, 1106. [[CrossRef](#)]
- Lee, G.F.; Rast, W.; Jones, R.A. Water Report: Eutrophication of water bodies: Insights for an age old problem. *Environ. Sci. Technol.* **1978**, *12*, 900–908. [[CrossRef](#)]

4. Tong, Y.; Bu, X.; Chen, C.; Yang, X.; Lu, Y.; Liang, H.; Liu, M.; Lin, H.; Zhang, H.; Lin, Y.; et al. Impacts of sanitation improvement on reduction of nitrogen discharges entering the environment from human excreta in China. *Sci. Total Environ.* **2017**, *593–594*, 439–448. [[CrossRef](#)] [[PubMed](#)]
5. Ministry of Housing and Urban Rural Development of the People's Republic of China. *China Urban Construction Statistical Yearbook*; Ministry of Housing and Urban Rural Development of the People's Republic of China: Beijing, China, 2020.
6. Barnard, J.L. Biological nutrient removal without the addition of chemicals. *Water Res.* **1975**, *9*, 485–490. [[CrossRef](#)]
7. Xu, R.; Fan, Y.; Wei, Y.; Wang, Y.; Luo, N.; Yang, M.; Yuan, X.; Yu, R. Influence of carbon sources on nutrient removal in A2/O-MBRs: Availability assessment of internal carbon source. *J. Environ. Sci.* **2016**, *48*, 59–68. [[CrossRef](#)]
8. Ekama, G.A.; Wentzel, M.C. Difficulties and developments in biological nutrient removal technology and modelling. *Water Sci. Technol.* **1999**, *39*, 1–11. [[CrossRef](#)]
9. Chen, P.; Wu, J.; Lu, X.; Yu, R. Denitrifying phosphorus removal and microbial community characteristics of two-sludge DEPHANOX system: Effects of COD/TP ratio. *Biochem. Eng. J.* **2021**, *172*, 108059. [[CrossRef](#)]
10. Shi, J.; Lu, X.; Yu, R.; Gu, Q.; Zhou, Y. Influence of wastewater composition on nutrient removal behaviors in the new anaerobic-anoxic/nitrifying/induced crystallization process. *Saudi J. Biol. Sci.* **2014**, *21*, 71–80. [[CrossRef](#)]
11. Fu, J.; Lin, Z.; Zhao, P.; Wang, Y.; He, L.; Zhou, J. Establishment and efficiency analysis of a single-stage denitrifying phosphorus removal system treating secondary effluent. *Bioresour. Technol.* **2019**, *288*, 121520. [[CrossRef](#)]
12. Wang, M.; Hu, S.; Wang, Q.; Liang, Y.; Liu, C.; Xu, H.; Ye, Q. Enhanced nitrogen and phosphorus adsorption performance and stabilization by novel panda manure biochar modified by CMC stabilized nZVZ composite in aqueous solution: Mechanisms and application potential. *J. Clean. Prod.* **2021**, *291*, 125221. [[CrossRef](#)]
13. Sui, Y.; Gao, J.; Liu, C.; Zhang, W.; Lan, Y.; Li, S.; Meng, J.; Xu, Z.; Tang, L. Interactive effects of straw-derived biochar and N fertilization on soil C storage and rice productivity in rice paddies of Northeast China. *Sci. Total Environ.* **2016**, *544*, 203–210. [[CrossRef](#)]
14. Lee, M.E.; Steiman, M.W.; St. Angelo, S.K. Biogas digestate as a renewable fertilizer: Effects of digestate application on crop growth and nutrient composition. *Renew. Agric. Food Syst.* **2021**, *36*, 173–181. [[CrossRef](#)]
15. Fytli, D.; Zabanitoutou, A. Utilization of sewage sludge in EU application of old and new methods—A review. *Renew. Sustain. Energy Rev.* **2008**, *12*, 116–140. [[CrossRef](#)]
16. Asai, H.; Samson, B.K.; Stephan, H.M.; Songyikhangsuthor, K.; Homma, K.; Kiyono, Y.; Inoue, Y.; Shiraiwa, T.; Horie, T. Biochar amendment techniques for upland rice production in Northern Laos: 1. Soil physical properties, leaf SPAD and grain yield. *Field Crops Res.* **2009**, *111*, 81–84. [[CrossRef](#)]
17. Piccolo, A.; Mbagwu, J.S.C. Effects of different organic waste amendments on soil microaggregates stability and molecular sizes of humic substances. *Plant Soil* **1990**, *123*, 27–37. [[CrossRef](#)]
18. Song, X.D.; Xue, X.Y.; Chen, D.Z.; He, P.J.; Dai, X.H. Application of biochar from sewage sludge to plant cultivation: Influence of pyrolysis temperature and biochar-to-soil ratio on yield and heavy metal accumulation. *Chemosphere* **2014**, *109*, 213–220. [[CrossRef](#)]
19. Yue, Y.; Cui, L.; Lin, Q.; Li, G.; Zhao, X. Efficiency of sewage sludge biochar in improving urban soil properties and promoting grass growth. *Chemosphere* **2017**, *173*, 551–556. [[CrossRef](#)]
20. Yuan, H.; Lu, T.; Wang, Y.; Chen, Y.; Lei, T. Sewage sludge biochar: Nutrient composition and its effect on the leaching of soil nutrients. *Geoderma* **2016**, *267*, 17–23. [[CrossRef](#)]
21. Ahmad, A.; Chowdhary, P.; Khan, N.; Chaurasia, D.; Varjani, S.; Pandey, A.; Chaturvedi, P. Effect of sewage sludge biochar on the soil nutrient, microbial abundance, and plant biomass: A sustainable approach towards mitigation of solid waste. *Chemosphere* **2022**, *287*, 132112. [[CrossRef](#)]
22. APHA. *Standard Methods for the Examination of Water and Wastewater*; APHA: Washington, DC, USA, 1998.
23. Sakhiya, A.K.; Vijay, V.K.; Kaushal, P. Efficacy of rice straw derived biochar for removal of Pb<sup>2+</sup> and Zn<sup>2+</sup> from aqueous: Adsorption, thermodynamic and cost analysis. *Bioresour. Technol. Rep.* **2022**, *17*, 100920. [[CrossRef](#)]
24. Shen, Z.; Hou, D.; Jin, F.; Shi, J.; Fan, X.; Tsang, D.C.W.; Alessi, D.S. Effect of production temperature on lead removal mechanisms by rice straw biochars. *Sci. Total Environ.* **2019**, *655*, 751–758. [[CrossRef](#)] [[PubMed](#)]
25. Gao, L.-Y.; Deng, J.-H.; Huang, G.-F.; Li, K.; Cai, K.-Z.; Liu, Y.; Huang, F. Relative distribution of Cd<sup>2+</sup> adsorption mechanisms on biochars derived from rice straw and sewage sludge. *Bioresour. Technol.* **2019**, *272*, 114–122. [[CrossRef](#)] [[PubMed](#)]
26. Rajec, P.; Rosskopfová, O.; Galamboš, M.; Frišták, V.; Soja, G.; Dafnomili, A.; Noli, F.; Đukić, A.; Matović, L. Sorption and desorption of pertechnetate on biochar under static batch and dynamic conditions. *J. Radioanal. Nucl. Chem.* **2016**, *310*, 253–261. [[CrossRef](#)]
27. Cheng, W.; Li, H.; Yang, Y.; Yin, B.; Bai, J.; Liu, H.; Liu, H. Preparation of biochar with fermented sludge residue by pyrolysis and adsorption of nitrogen and phosphorus. *CIESC J.* **2016**, *67*, 1541–1548. [[CrossRef](#)]
28. Xu, X.; Zhao, Y.; Sima, J.; Zhao, L.; Mašek, O.; Cao, X. Indispensable role of biochar-inherent mineral constituents in its environmental applications: A review. *Bioresour. Technol.* **2017**, *241*, 887–899. [[CrossRef](#)] [[PubMed](#)]
29. Zhang, H.; Voroney, R.P.; Price, G.W. Effects of temperature and processing conditions on biochar chemical properties and their influence on soil C and N transformations. *Soil Biol. Biochem.* **2015**, *83*, 19–28. [[CrossRef](#)]
30. Zhao, L.; Cao, X.; Mašek, O.; Zimmerman, A. Heterogeneity of biochar properties as a function of feedstock sources and production temperatures. *J. Hazard. Mater.* **2013**, *256–257*, 1–9. [[CrossRef](#)]

31. Chen, B.; Zhou, D.; Zhu, L. Transitional adsorption and partition of nonpolar and polar aromatic contaminants by biochars of pine needles with different pyrolytic temperatures. *Environ. Sci. Technol.* **2008**, *42*, 5137–5143. [[CrossRef](#)]
32. Wang, H.; Wang, X.; Zhao, X. Synthesis and characterization of novel fluorine-containing water-based antirust coating. *IOP Conf. Ser. Mater. Sci. Eng.* **2018**, *301*, 012005. [[CrossRef](#)]
33. Guo, Q. *Polymer Morphology: Principles, Characterization and Processing*; John Wiley & Sons, Inc.: Hoboken, NJ, USA, 2016.
34. Chia, C.H.; Gong, B.; Joseph, S.D.; Marjo, C.E.; Munroe, P.; Rich, A.M. Imaging of mineral-enriched biochar by FTIR, Raman and SEM–EDX. *Vib. Spectrosc.* **2012**, *62*, 248–257. [[CrossRef](#)]
35. Keiluweit, M.; Nico, P.S.; Johnson, M.G.; Kleber, M. Dynamic molecular structure of plant biomass-derived black carbon (biochar). *Environ. Sci. Technol.* **2010**, *44*, 1247–1253. [[CrossRef](#)]
36. Suhua, G.; Zhongjian, X.; Fangwen, L.; Dandan, X. Adsorption of Pb(II), Zn(II) from aqueous solution by biochars. *Chin. J. Environ. Eng.* **2015**, *9*, 3215–3222. [[CrossRef](#)]
37. Agrafioti, E.; Bouras, G.; Kalderis, D.; Diamadopoulos, E. Biochar production by sewage sludge pyrolysis. *J. Anal. Appl. Pyrolysis* **2013**, *101*, 72–78. [[CrossRef](#)]
38. Chuan, S.; Panyue, Z.; Guo, J.; Zhang, G. Phosphorus adsorption performance onto sewage sludge biochar. *Chin. J. Environ. Eng.* **2016**, *10*, 7202–7208. [[CrossRef](#)]
39. Guo, H.; Chunxia, H.E. Study on physicochemical properties of four biochars and their adsorption to methylene Blue. *Dev. Appl. Mater.* **2019**, *34*, 113–119. [[CrossRef](#)]
40. Yavari, S.; Malakahmad, A.; Sapari, N.B. Biochar efficiency in pesticides sorption as a function of production variables-A review. *Environ. Sci. Pollut. Res.* **2015**, *22*, 13824–13841. [[CrossRef](#)]
41. Chen, Y.; Zhang, X.; Chen, W.; Yang, H.; Chen, H. The structure evolution of biochar from biomass pyrolysis and its correlation with gas pollutant adsorption performance. *Bioresour. Technol.* **2017**, *246*, 101–109. [[CrossRef](#)]
42. Odedishemi Ajibade, F.; Wang, H.-C.; Guadie, A.; Fausat Ajibade, T.; Fang, Y.-K.; Muhammad Adeel Sharif, H.; Liu, W.-Z.; Wang, A.-J. Total nitrogen removal in biochar amended non-aerated vertical flow constructed wetlands for secondary wastewater effluent with low C/N ratio: Microbial community structure and dissolved organic carbon release conditions. *Bioresour. Technol.* **2021**, *322*, 124430. [[CrossRef](#)]
43. Yao, Y.; Gao, B.; Inyang, M.; Zimmerman, A.R.; Cao, X.; Pullammanappallil, P.; Yang, L. Removal of phosphate from aqueous solution by biochar derived from anaerobically digested sugar beet tailings. *J. Hazard. Mater.* **2011**, *190*, 501–507. [[CrossRef](#)]
44. Chitrakar, R.; Tezuka, S.; Sonoda, A.; Sakane, K.; Ooi, K.; Hirotsu, T. Selective adsorption of phosphate from seawater and wastewater by amorphous zirconium hydroxide. *J. Colloid Interface Sci.* **2006**, *297*, 426–433. [[CrossRef](#)] [[PubMed](#)]
45. Tan, Z.; Yuan, S.; Hong, M.; Zhang, L.; Huang, Q. Mechanism of negative surface charge formation on biochar and its effect on the fixation of soil Cd. *J. Hazard. Mater.* **2020**, *384*, 121370. [[CrossRef](#)] [[PubMed](#)]
46. Yuan, H.Y.; Zhang, H.X.; Chen, Y.G.; Zhou, Q. Impact of pH on the generation of COD, phosphorous and ammonia-nitrogen during the anaerobic fermentation of excess activated sludge. *Huan Jing Ke Xue* **2006**, *27*, 1358–1361. [[CrossRef](#)]
47. Chang, M.-Y.; Juang, R.-S. Adsorption of tannic acid, humic acid, and dyes from water using the composite of chitosan and activated clay. *J. Colloid Interface Sci.* **2004**, *278*, 18–25. [[CrossRef](#)] [[PubMed](#)]
48. Ofomaja, A.E.; Naidoo, E.B.; Modise, S.J. Dynamic studies and pseudo-second order modeling of copper(II) biosorption onto pine cone powder. *Desalination* **2010**, *251*, 112–122. [[CrossRef](#)]
49. Shin, E.W.; Han, J.S.; Jang, M.; Min, S.-H.; Park, J.K.; Rowell, R.M. Phosphate adsorption on aluminum-impregnated mesoporous silicates: Surface structure and behavior of adsorbents. *Environ. Sci. Technol.* **2004**, *38*, 912–917. [[CrossRef](#)]
50. Chung, H.-K.; Kim, W.-H.; Park, J.; Cho, J.; Jeong, T.-Y.; Park, P.-K. Application of Langmuir and Freundlich isotherms to predict adsorbate removal efficiency or required amount of adsorbent. *J. Ind. Eng. Chem.* **2015**, *28*, 241–246. [[CrossRef](#)]
51. Doumer, M.E.; Rigol, A.; Vidal, M.; Mangrich, A.S. Removal of Cd, Cu, Pb, and Zn from aqueous solutions by biochars. *Environ. Sci. Pollut. Res.* **2016**, *23*, 2684–2692. [[CrossRef](#)]